AIP | Journal of Applied Physics

Area-scaling of organic solar cells

Seungkeun Choi, William J. Potscavage, and Bernard Kippelen

Citation: J. Appl. Phys. **106**, 054507 (2009); doi: 10.1063/1.3211850
View online: http://dx.doi.org/10.1063/1.3211850
View Table of Contents: http://jap.aip.org/resource/1/JAPIAU/v106/i5
Published by the American Institute of Physics.

Area-scaling of organic solar cells

Seungkeun Choi, William J. Potscavage, Jr., and Bernard Kippelen[a)]
Center for Organic Photonics and Electronics (COPE) and School of Electrical and Computer Engineering, Georgia Institute of Technology, Atlanta, Georgia 30332, USA

(Received 14 May 2009; accepted 28 July 2009; published online 4 September 2009)

We report on the performance of organic solar cells based on pentacene/C_{60} heterojunctions as a function of active area. Devices with areas of 0.13 and 7 cm^2 were fabricated on indium-tin-oxide (ITO) coated glass. Degradation of the performance with increased area is observed and analyzed in terms of the power loss density concept. The various power loss contributions to the total series resistance (R_SA) are measured independently and compared to the values of the series resistance extracted from the current-voltage characteristics using a Shockley equivalent circuit model. The limited sheet resistance of ITO is found to be one of the major limiting factors when the area of the cell is increased. To reduce the effects of series resistance, thick, electroplated, metal grid electrodes were integrated with ITO in large-area cells. The metal grids were fabricated directly onto ITO and passivated with an insulator to prevent electrical shorts during the deposition of the top Al electrode. By integrating metal grids onto ITO, the series resistance could be reduced significantly yielding improved performance. Design guidelines for metal grids are described and tradeoffs are discussed.
 [doi:10.1063/1.3211850]

I. INTRODUCTION

Organic photovoltaics have received great interest in recent years due to the promising potential for the development of large-area, low-cost, light-weight solar modules with highly flexible form factors.[1] Significant efforts have been focused on improving the power conversion efficiency through the synthesis of new light-harvesting molecules and polymers[2–4] and through tandem cell architectures.[5] The power conversion efficiency is defined by

$$\eta = \frac{J_{\max} V_{\max}}{P_{\text{inc}}} = \text{FF} \frac{J_{\text{SC}} V_{\text{OC}}}{P_{\text{inc}}}, \tag{1}$$

where P_{inc} is the incident power density, $J_{\max}$ and $V_{\max}$ are the current density and voltage, respectively, at which the maximum power is generated in the device, FF denotes the fill factor, J_{SC} is the short-circuit current density, and V_{OC} is the open-circuit voltage. However, less attention has been given to understanding how the power conversion efficiency scales with device area, and reports dealing with this important issue are relatively scarce.[6,7]

Because solar cells, like all electronic devices, exhibit series resistances that can never be completely avoided, some generated power will be lost by dissipation through the internal resistance of the device. Therefore, another important quantity to consider in the optimization of the efficiency of a cell is the total resistive power loss per unit area P_R, which is given by

$$P_R = \frac{R_S I_{\max}^2}{A} = \frac{R_S (J_{\max} A)^2}{A} = R_S A J_{\max}^2, \tag{2}$$

where R_S is the series resistance in the device and A is the area of the device. Equation (2) clearly illustrates that the resistive power loss per unit area is proportional to the series resistance (R_SA) and that consequently the effects of parasitic series resistance are likely to play a more prominent role as the area of the cell is increased. Therefore, methods are needed to evaluate this power loss and relate it to the performance of solar cells.

In this paper, we present a study of the area-scaling of organic solar cells based on pentacene/C_{60} heterojunctions[8] with active areas of 0.13 and 7 cm^2. The current-voltage (J-V) characteristics of these devices are fitted using an equivalent circuit model that relates the parameters of the model to physical characteristics of the cell. The model allows one to study the effects of the value of each parameter on the J-V characteristics and consequently on the power conversion efficiency by simple numerical simulation.

Power loss calculations show that the organic semiconductors contribute more to the resistive power loss than the indium-tin-oxide (ITO) in small-area devices. However, power loss from the ITO is the only area-scaling parameter. Based on the power loss analysis, we propose electroplated metal grids which are integrated with the ITO layer as a route to reduce the resistive losses.

The grid structures are passivated with photoresist to prevent electrical shorts between the ITO and the metal electrode. Even though the metal grid structures introduce additional power losses such as contact loss between the ITO and the metal, resistive power losses from the grid itself, and shadow power loss, overall resistive power loss is reduced because of the reduced power loss from the ITO layer. Improved performance of large-area devices with an integrated metal grid is enabled by reduced R_S for these devices, as calculated from the equivalent circuit model. Finally, we show the effects of R_S on the overall solar cell performance by using the equivalent circuit model.

[a)]Author to whom correspondence should be addressed. Electronic mail: kippelen@ece.gatech.edu.

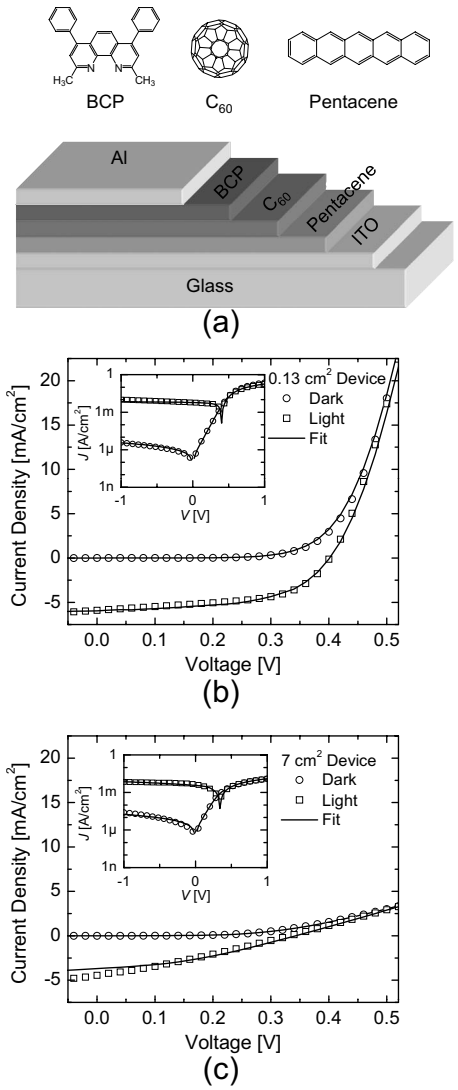

FIG. 1. (a) Device geometry. (b) Experimental (shapes) and fitted (solid lines) *J-V* characteristics for a small-area device in the dark (circles) and under illumination (squares). Inset: full range curves on semilogarithmic scale. (c) The same for a large-area device.

II. SMALL-AREA AND LARGE-AREA ORGANIC SOLAR CELL FABRICATION AND TESTING

To understand how area-scaling affects the performance of organic solar cells, small-area and large-area solar cells based on pentacene/C_{60} heterojunctions with active areas of 0.13 (small area) and 7 cm^2 (large area) were fabricated. The devices under study consisted of pentacene as the donor, C_{60} as the acceptor, and bathocuproine (BCP) as an exciton-blocking layer. The device geometry was ITO/pentacene (50 nm)/C_{60} (45 nm)/BCP (8 nm)/Al, as shown in Fig. 1(a).[8,9] All of the organic materials were purified at least once by thermal gradient sublimation.[10] ITO-coated glass (Colorado Concept Coatings LLC) with a specified sheet resistance of $\sim$15 Ω/sq was used as the substrates. The organic layers and Al were deposited by vacuum thermal evaporation without breaking vacuum between depositions. Active areas of 0.13 and 7 cm^2 were created by patterning the ITO and depositing the Al through a shadow mask. The active area of the ITO was 0.46 cm in length and 0.28 cm in width for the small-area device and 2.85 cm in length and 2.45 cm in width for the large-area device. Unlike the small-area devices, the large-area cell had contacts to the ITO at both ends of the cell, which will be discussed in more detail later. The photovoltaic properties were measured in ambient air. An AM1.5G solar simulator (Oriel, 91160) was used as the light source, and the intensity of the incident light was measured with a thermal optical power sensor (detector area =2.85 cm^2). The *J-V* characteristics were measured with a Keithley 2400 source meter in a four-wire connection scheme.

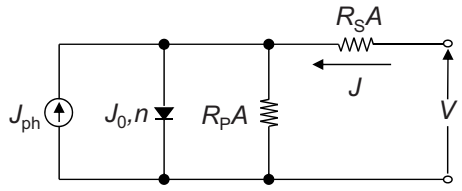

FIG. 2. Equivalent circuit model (Ref. 9).

J-V characteristics for the small-area device are shown in Fig. 1(b) in the dark and under illumination. The short-circuit current density (J_{SC}) and open-circuit voltage (V_{OC}) were 6.0 mA/cm^2 and 401 mV under an illumination of $\sim$104 mW/cm^2. A FF of 0.54 yields a power-conversion efficiency of 1.2% for the small-area device. These results are in the range of what has been reported previously for pentacene/C_{60} solar cells.[8,11–13]

Figure 1(c) shows the *J-V* curves for the large-area cell in the dark and under illumination. Efficiency significantly drops for the large-area cell and is only about one-third that of the small-area cell at 0.41%. The decrease in efficiency is caused by decreases in all of the performance parameters. FF decreased by almost half and is 0.29 for the large-area device compared to 0.54 for the small-area device. J_{SC} and V_{OC} also declined significantly to 4.5 mA/cm^2 and 338 mV for the large-area device. To begin to explain the large differences in performance between the two cells, the equivalent circuit model will be used as a means to parametrize the *J-V* curves with terms that can be related to physical properties in the solar cells.

III. EQUIVALENT CIRCUIT MODEL

The *J-V* characteristics of organic solar cells can be studied in more detail by fitting and parameterizing the curves with the equivalent circuit model. Because the parameters of the model can be related to different processes in the cell, the effect of specific aspects of the cell architecture on performance can be predicted, and the most critical aspects can be targeted for improvement. While the equivalent circuit model was originally developed for inorganic solar cells, it has been found to be also applicable to organic solar cells.[9,14]

The equivalent circuit is shown in Fig. 2 and consists of a diode, a dc current source, a shunt resistance, and a series resistance. The diode represents the behavior of an ideal solar cell in the dark and is parameterized with an ideality factor n and a reverse saturation current density J_0. The dc current source represents the photocurrent density J_{ph} generated when the solar cell is illuminated. A shunt resistance R_P

TABLE I. Comparison of equivalent circuit model parameters for the small- and large-area devices. L and W are the length and width of the solar cell, respectively. α depends on the interconnect contact geometry (refer to Fig. 4). J_0 and n are the reverse saturation current density and ideality factor of the diode, respectively. R_SA and R_PA are the series and shunt resistance in the equivalent circuit model (refer to Fig. 2).

Parameter	Small-area device (0.13 cm^2)		Large-area device (7 cm^2)	
L (cm)	0.46		2.85	
W (cm)	0.28		2.45	
α	3		12	
	In the dark	Under illumination	In the dark	Under illumination
J_0 (μA/cm^2)	0.22	0.02	0.80	0.01
n	1.59	1.28	1.68	1.02
R_SA (Ω cm^2)	2.1	2.8	49.2	52.1
R_PA (Ω cm^2)	221 000	361	64 100	157

is included to account for leakage in the diode from sources such as pinholes and recombination. Finally, the series resistance R_S is related to the finite resistance of the bulk materials of the diode, the resistance of the electrodes, and the contact resistances between adjacent layers. With the knowledge of a given set of parameters $\{n, J_0, J_{ph}, R_S, R_P\}$, the J-V characteristics can be simulated with the equation

$$J = J_0\left\{\exp\left(\frac{V - JR_SA}{nkT/e}\right) - 1\right\} + \frac{V - JR_SA}{R_PA} - J_{ph}, \qquad (3)$$

where A is the active area, k is the Boltzmann constant, T is the temperature, and e is the elementary charge. Hence, the effects of the value of each parameter on the J-V characteristics and consequently on the power conversion efficiency can be simulated numerically very easily.

The parameters n, J_0, J_{ph}, R_P, and R_S can all be extracted from the J-V measurements of a device by fitting the model to experimental data.[9] Estimates of R_S and R_P can be found from the inverse slopes of the forward and reverse characteristics, respectively.[15] When fitting data in the dark, the estimates of R_S and R_P can be used to effectively remove the effect of the resistances on the diode by defining $V' = V - JR_SA$ and $J' = J - V'/R_PA$. J_0 and n can then be calculated from the y-intercept and slope, respectively, of a straight line fit to the linear portion of $\ln(J')$ versus V' in the forward bias. When fitting data under illumination, the additional experimental parameters of FF and J_{SC} are used, and J_0 and n can then be calculated as the values that give the same FF and J_{SC} as measured experimentally for the given estimates of R_S and R_P. R_S and R_P are then varied until the minimum of a sum of least squares between the experimental and fitted values over the entire curve is found. It should be noted that because current density will be compared between devices with different areas to facilitate comparison of the device characteristics, R_SA and R_PA are used hereafter to represent the series resistance and the shunt resistance, respectively.

Fits to the equivalent circuit model are shown in Figs. 1(b) and 1(c) as solid lines for the small-area and large-area devices, respectively. The parameters for the fits are listed in Table I. It is clear from the graphs that the model fits the experimental data well over the entire range of voltages from −1 to 1 V both in the dark and under illumination. This model is especially useful because the entire curve can be described with only five parameters, which prevents the model from becoming too complex. Looking at the parameters in Table I, the R_SA and R_PA change the most between the two devices. R_SA increases more than 23-fold while the R_PA decreases as much as threefold when the active area increases from 0.13 to 7 cm^2. Upon illumination, both devices exhibit slightly increased series resistance and greatly reduced shunt resistance, and R_SA is clearly the most impacted parameter as area is increased.

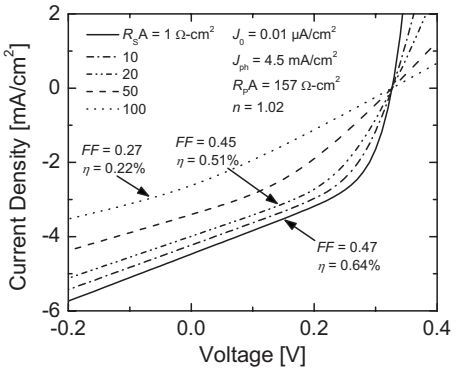

FIG. 3. Effect of series resistance (R_SA) on organic photovoltaic performance.

The equivalent circuit model can be used to verify that a change in series resistance can have such a strong influence on device performance by varying the R_SA and holding the other parameters constant. Figure 3 illustrates how changing the R_SA affects the shape of the J-V curves using the model parameters for the large-area device. The graphs show that J_{SC} and the current density and voltage at which maximum power is produced are all lowered as R_SA increases substantially. These effects result in a lower maximum power output and FF for the cell, therefore decreasing the efficiency. According to Eq. (2), an increase in R_SA is also expected to increase the amount of generated power lost through resistive dissipation, thereby lowering efficiency. To design efficient solar cells with large areas, the mechanisms that contribute to the series resistance and power loss as cell area is increased must be understood.

IV. ANALYSIS OF POWER LOSS AND SERIES RESISTANCE

Knowing where power is lost in a solar cell and how the device geometry and structure affect the power loss and series resistance is important for the design of large-area solar cells. Calculating power loss densities of various resistive layers of a solar cell has been used to analyze the electrical characteristics of both inorganic and organic solar cells.[6,16] The resistive power loss density depends on the resistivities of the electrodes and the organic semiconductors and the contacts between film interfaces,[17] and is given by

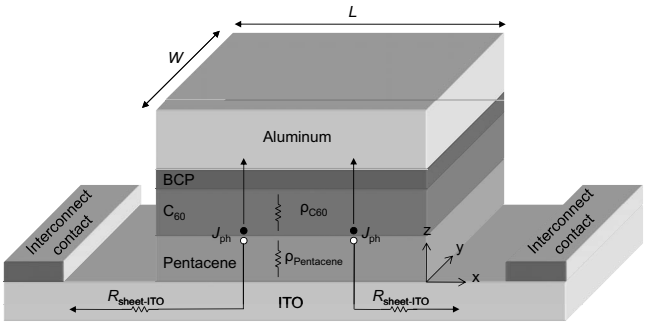

FIG. 4. Description of current flow in organic solar cells. Current flow on the x-y plane contributes to the area-scaling loss while current flow along the z axis does not.

$$P_R = P_{\mathrm{ITO}} + P_{\mathrm{organic}} + P_{\mathrm{contacts}} + P_{\mathrm{Al}}, \tag{4}$$

where P_{ITO} and P_{organic} are the resistive power loss densities of the ITO and organic semiconductors, respectively. P_{contacts} include all the interfacial contact power loss densities between films, such as metal-organic and organic-organic interfaces. P_{Al} is the resistive power loss of the cathode, which is aluminum in this case.

For a device structure as shown in Fig. 4, the power loss density of the ITO layer (P_{ITO}) is given by[18]

$$P_{\mathrm{ITO}} = \frac{1}{\alpha} J_{\mathrm{max}}^2 L^2 R_{\text{sheet-ITO}}, \tag{5}$$

where $R_{\text{sheet-ITO}}$ is the sheet resistance of the ITO in Ω/sq, L is the length of the solar cell, and α is determined by the number of interconnect contacts. For example, α is 3 when only one of the interconnect contacts is used, whereas it is 12 when both contacts are used. Details of the calculation can be found in the Appendix. It is assumed that all of the generated current flows in a direction normal to the edge. Therefore, solar cell width (W) does not affect the power loss density. Note that by utilizing both contacts along the opposite edges, the losses are considerably reduced.[19] In this research, the small-area device has only one interconnect contact due to its small size while the large-area device utilizes two contacts on both edges, as shown in Fig. 4. The power loss density of the organic semiconductors can be calculated the same way as for the bulk layer in silicon solar cells and is given by[18]

$$P_{\mathrm{organic}} = J_{\mathrm{max}}^2 (\rho_{\mathrm{pentacene}} t_{\mathrm{pentacene}} + \rho_{\mathrm{C_{60}}} t_{\mathrm{C_{60}}}), \tag{6}$$

where ρ is the resistivity in Ω cm and t is the thickness of the organic semiconductor layers (Fig. 4).

Equations (5) and (6) show that the power loss density from the ITO depends on the length of the active area along which photogenerated current flows, whereas the power loss density of the organic semiconductors is not a function of area. In fact, power loss density increases with area only when the photogenerated current flows in the x-y plane (Fig. 4) of the active area, i.e., the ITO or cathode, since increasing the active area makes the photogenerated current travel a longer distance before it is collected at the external electrodes, thereby increasing series resistance. Furthermore, the position of the contacts in the devices here causes current to flow primarily in the x-direction, so P_{ITO} depends on only L and not W. On the other hand, the resistive components of the organic solar cell in which the photogenerated current flows perpendicular (z-direction in Fig. 4) to the active area do not contribute to the area-dependent power loss density since increasing the area does not increase the path that the current travels. Instead, the power loss density of the organic semiconductors depends only on the film thickness, as shown in Eq. (6).

Looking at the remaining terms in Eq. (4), the power loss density from interfacial contacts does not scale with area because it is z-direction component. Power loss from the cathode electrode (P_{Al}) scales with area since the photogenerated current flows along the x-y plane of the cathode. However, its contribution to the power loss is ignored here because of its relatively higher conductance compared to ITO. Furthermore, its resistive power loss can be reduced by simply increasing the cathode thickness.

Resistive power losses affect the performance of the solar cell by increasing the series resistance,[20] which is given by rewriting Eq. (2),

$$R_S A = \frac{P_R}{J_{\mathrm{max}}^2}. \tag{7}$$

At a given photogenerated current density, the value of $R_S A$ is proportional to the resistive power losses. $R_S A$ for these devices can be calculated by combining Eqs. (4)–(7) as

$$R_S A = \frac{1}{\alpha} L^2 R_{\text{sheet-ITO}} + (t_{\mathrm{pentacene}} \rho_{\mathrm{pentacene}} + t_{\mathrm{C_{60}}} \rho_{\mathrm{C_{60}}}). \tag{8}$$

Because of the dependence on L^2 from the ITO component, $R_S A$ will increase with the length of the device. It is well known that the series resistance is a parameter which can limit the performance of a solar cell by reducing both FF and photocurrent for both inorganic and organic solar cells.[20–26] Therefore, the effective series resistance of the ITO film must be minimized to prevent the overall power conversion efficiency from decreasing as the area increases.

V. ANALYSIS OF SERIES RESISTANCE WITH GRID ELECTRODE

One way to decrease the overall resistance of the anode is by fabricating metal grids on top of the anode that can provide an alternative, low-resistance pathway for current. The metallic grids consist of finger electrodes branching out from a busbar electrode, as shown in Fig. 5. Photogenerated current travels through the ITO, gets collected by the nearest finger electrode, and then is delivered into the busbar electrode, which is connected directly to the external leads. Such a grid has been demonstrated with a poly(3,4-ethylenedioxythiophene):poly(styrenesulfonate) (PEDOT:PSS) film as the anode in an attempt to develop a transparent anode that is a cheaper alternative to ITO.[27–30] While the PEDOT:PSS alone can act as a transparent anode, a grid was needed to lower the series resistance because PEDOT:PSS has a significantly higher resistance relative to ITO. In this research, the grid will be applied to maintain a low effective resistance of the ITO even as the area of the solar cell be-

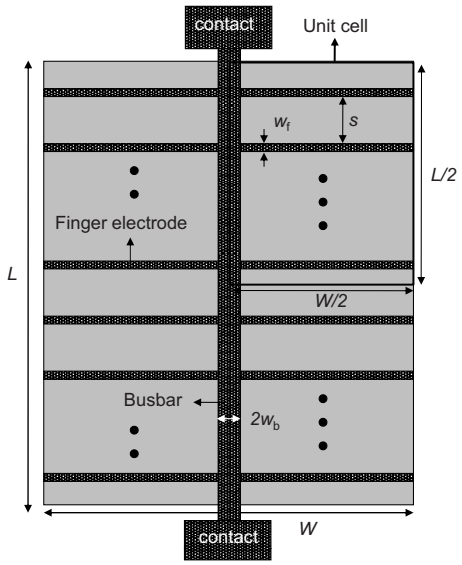

FIG. 5. Large-area solar cell with a grid. The unit cell is defined such that the total photogenerated current leaves the unit cell only through the busbar and no photogenerated current flows across any of the unit cell edges.

comes large. This approach could also be applied to other cheaper transparent electrodes that are not ITO in the future.

Metal grids are also used in conventional silicon solar cells and are placed on top of the *n*-type semiconductor as a cathode. The grid can be placed on top because no transparent electrode covering the entire area is needed since the *n*-type semiconductor is sufficiently conducting in the plane of the device to act as a moderately resistive cathode. Since the silicon wafer is between the metal grid and the anode, which coats the back of the wafer, both electrodes are well isolated.[31] Considering Fig. 1(a), the grid for an organic device must be fabricated directly on top of the ITO with the organic layers and cathode subsequently deposited. An additional passivation is therefore needed on top of the metal grid because the thin organic layers (~100 nm) might not adequately coat the thick metal grid (~3.4 μm) to isolate the grid from the cathode.

The power loss densities of a solar cell with an integrated metal grid must be studied to verify that the grid structure can decrease losses and increase efficiency. In addition to the resistive power losses of the ITO and organic semiconductors, the metal grid structure introduces additional power losses such as contact loss between the ITO and the grid, resistive power losses from the grid itself, and a shadow power loss. The shadow power loss is associated with shadow areas, which are created by the metal grid blocking the incoming sunlight. As with the devices without a grid, the total resistive power loss density can be written as a sum of power loss densities for a device with a grid,

$$P_R^{\text{grid}} = P_{\text{ITO}}^{\text{grid}} + P_{\text{organic}} + P_{\text{contacts}} + P_{\text{Al}} + P_{\text{finger}} + P_{\text{busbar}}, \tag{9}$$

where $P_{\text{ITO}}^{\text{grid}}$ is the power loss density from the ITO when a grid is present, and P_{finger} and P_{busbar} are the power densities dissipated in the fingers and busbars of the grid, respectively.

TABLE II. Contributions to R_SA for the unit cell in a solar cell with metal grids. P_{shadow} is the shadow power loss density. The units used for the power loss densities are mW/cm^2. J_{max} and V_{max} are the photogenerated current density and voltage at the maximum power generation point. $R_{\text{sheet-ITO}}$ is the sheet resistance of the ITO in Ω/sq. s is the space between finger electrodes. R_{smf} and R_{smb} are the sheet resistance of the metal finger electrodes and busbar, respectively. r_{specific} is the specific contact resistance in Ω cm^2 between the ITO and the copper grids. $\rho_{\text{pentacene}}$ and $\rho_{C_{60}}$ are the resistivity of the pentacene and C_{60}, respectively. $t_{\text{pentacene}}$ and $t_{C_{60}}$ are the film thickness of the pentacene and C_{60}, respectively. w_f and w_b are the width of the finger electrodes and busbar electrode, respectively. Refer to Ref. 19 and Fig. 5 for further details.

Contributor	R_SA (Ω cm^2)	Contributor	R_SA (Ω cm^2)
ITO	$\frac{1}{12}R_{\text{sheet-ITO}}s^2$	Contact	$r_{\text{specific}}\frac{s}{w_f}$
Finger electrode	$\frac{1}{12}W^2R_{\text{smf}}\frac{s}{w_f}$	Organic layers	$(\rho_{\text{pentacene}}t_{\text{pentacene}}+\rho_{C_{60}}t_{C_{60}})$
Busbar	$\frac{1}{24}L^2W\frac{R_{\text{smb}}}{w_b}$	P_{shadow} (mW/cm^2)	$J_{\text{max}}V_{\text{max}}\left(\frac{w_f}{s}+2\frac{w_b}{W}\right)$

As with the devices without a grid, the power loss density from the Al cathode will be neglected.

Power loss densities of a solar cell with an integrated metal grid can be calculated based on the unit cell concept.[19] The unit cell is defined such that the total photogenerated current leaves the unit cell only through the busbar and no photogenerated current flows across any of the unit cell edges. The individual power loss calculations for each component of the unit cell are well explained elsewhere,[19,31] and the corresponding series resistance equations calculated from the power loss densities using Eq. (7) are summarized in Table II for a grid with the geometry shown in Fig. 5. The power loss density is calculated based on the J_{max} and V_{max}, and it is assumed that J_{max} is uniform over the cell surface. However, the series resistance (R_SA) is not affected by either the J_{max} or V_{max} and is obtained by adding all series resistances in Table II and given by

$$R_S^{\text{grid}}A = \frac{1}{12}s^2R_{\text{sheet-ITO}} + (t_{\text{pentacene}}\rho_{\text{pentacene}} + t_{C_{60}}\rho_{C_{60}}) + \frac{r_{\text{specific}}s}{w_f} + \frac{W^2R_{\text{smf}}s}{12w_f} + \frac{L^2WR_{\text{smb}}}{24w_b}, \tag{10}$$

where each of the terms, from left to right, represents the series resistances of the ITO, the organic layers, the ITO/Cu interface, the finger electrodes, and the busbar electrode. It is worth mentioning that power loss density should not be used for comparison when J_{max} of the devices is not the same. Instead, R_SA should be used in that case because it does not depend on J_{max}.

Equation (10) can now be compared to Eq. (8) to see how series resistance differs for the devices with and without a grid. The first term in each equation accounts for the resistance from the ITO. When the grid is included, the ITO resistance scales only with the spacing between the finger electrodes s instead of with the length of the entire device L. Thus, the contribution to resistance from the ITO for a large-area device can be significantly decreased and will not de-

pend on area when a grid is used as long as the finger electrode spacing is small. However, introduction of the grid adds three new terms for the resistance of the finger electrodes and busbar of the grid and for the contact resistance between the grid and ITO. All three terms will depend on the spacing and width of the finger electrodes or the width of the busbars. While the terms for the finger electrode and busbar resistance depend on the unit cell area of the cell, they can be kept small because of the low resistivity of the metal. Ideally, the performance of solar cells with a grid should not depend on the area as long as the cell keeps the same unit cell dimension with negligible grid resistance as the area increases. Finally, resistance from the organic layers does not change because the current flows in the z-direction.

While most of the variables in Eq. (10) come from the geometry or material properties, one additional parameter that must be measured is the specific contact resistance r_{specific} between the ITO and the metal grid. The transfer length method (TLM), sometimes called the transmission line method, is often used to measure specific contact resistance ($r_{\text{specific}}, \Omega\,\text{cm}^2$) and sheet resistance ($\Omega/\text{sq}$) simultaneously.[32] Specific contact resistance is widely used since it is independent of the contact geometry.[33] Specific contact resistance includes not only the actual interface but also the regions immediately above and below the interface.[32] To find r_{specific}, the total resistance is first measured between consecutive electrodes on a conducting strip with varying lengths l between each electrode. The total resistance (R_{tot}) between any two adjacent electrodes is given by[32]

$$R_{\text{tot}} = \frac{R_{\text{sheet}}}{W_d} l + 2R_C, \tag{11}$$

where R_{sheet} is the sheet resistance of the conducting strip in Ω/sq, W_d is the width of the electrodes, l is the space between electrodes, and R_C is the contact resistance in ohm. The specific contact resistance (r_{specific}) is given by[32]

$$r_{\text{specific}} = \frac{R_C^2 W_d^2}{R_{\text{sheet}}}. \tag{12}$$

The sheet resistance of the ITO can be calculated from Eq. (11) by multiplying the slope of the graph of l versus R_{tot} with the electrode width (W_d).

VI. METAL GRID ELECTRODE FABRICATION AND CHARACTERIZATION

In this research, a metal grid fabricated on top of ITO by electroplating was used as the anode for a large-area solar cell. ITO-coated glass was diced into 1.5×1.5 in.^{2} substrates, and an active area of 7 cm^2 was created by patterning the ITO using chemical wet etching. Then, the ITO was cleaned in sequential ultrasonic baths of soap, acetone, and isopropanol for 60 min each. Seed layers consisting of 20 nm of chromium and 200 nm of copper were deposited over the entire ITO surface using a filament evaporator. Electroplating mold structures were created with a thick photoresist (Shipley SPR220). Copper plating solution was prepared by mixing 250 mg $CuSO_4{-}5H_2O$ and 25 ml H_2SO_4 in 1 liter of

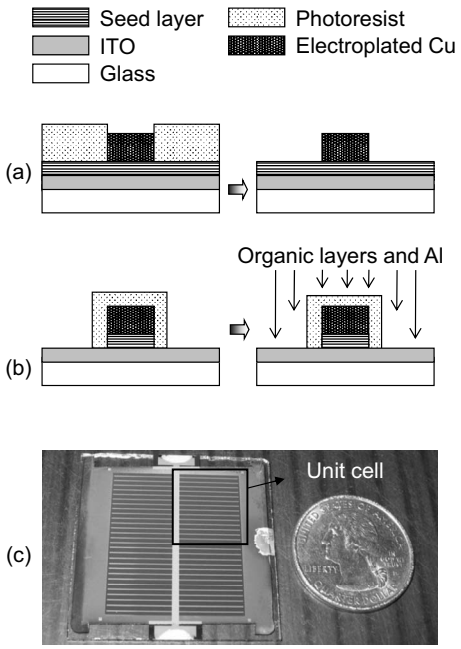

FIG. 6. Fabrication sequence: (a) ITO patterning, seed layer deposition (chrome 20 nm and copper 200 nm), mold structure creation, and copper electroplating; (b) metal grid passivation, seed layer removal, and organic layers and cathode electrode deposition; (c) complete device.

de-ionized water.[34] 3.4 μm of copper was electroplated by applying a dc current density of 15 mA/cm^2 [Fig. 6(a)]. The molding structures were removed using a photoresist remover (Shipley Microposit Remover 1165 at 80 °C for 10 min). Photoresist (Futurex NR9-8000P) was used to form a passivation layer on top of electroplated grids [Fig. 6(b)]. The passivated area accounts for 14.3% of the ITO area. Finally, the chromium and copper seed layers were removed by wet chemical etching. By removing the seed layer in the last step of the fabrication, the ITO surface is protected from possible contamination during the passivation process. Before organic semiconductor deposition, the ITO surface was treated with oxygen plasma[35] and phosphoric acid[36] (20% P_3HO_4 for 10 min). After rinsing with de-ionized water and drying on a hotplate, the devices were transferred into a vacuum thermal evaporator (Spectros, Kurt J. Lesker), and the organic layers and aluminum were deposited without breaking the vacuum in the same batch as the large-area device without a grid. The photovoltaic properties were measured in ambient air under an AM1.5G solar simulator (Oriel, 91160) with an irradiance $I_L = 108$ mW/cm^2 and in the dark. The fabrication sequence and geometry of the device are shown in Fig. 6. The dimensions and parameters of the fabricated device are listed in Table III.

To measure the specific contact resistance, TLM patterns were created in which 15 electroplated copper contacts are arranged with different spacing on an ITO strip [Fig. 7(a)]. Three different ITO strips with TLM patterns were fabricated and measured. ITO was patterned and copper contact electrodes were fabricated with the same processes that were used for the metal grid of the large-area solar cell.

VII. RESULTS AND DISCUSSION

To calculate the various contributions to series resistance, all of the parameters in Eqs. (8) and (10) first had to be

TABLE III. Dimensions and parameters of the metal grid integrated large-area solar cell. $r_{specific}$, R_{smf}, and R_{smb} represent the specific contact resistance and sheet resistance of the finger electrode and busbar electrode, respectively. The unit cell is 1.42 cm in length and 1.23 cm in width (Fig. 5).

Parameter	Value	Parameter	Value
L (cm)	2.85	$r_{specific}$ ($\mu\Omega$ cm^2)	117
W (cm)	2.45	$R_{sheet\text{-}ITO}$ (Ω/sq)	13.7
J_{max} (mA/cm^2)	3.6	R_{smf} (Ω/sq)	0.006
V_{max} (V)	0.23	R_{smb} (Ω/sq)	0.006
w_f (μm)	50	$(\rho t)_{pentacene}$ (Ω cm^2) [a]	1.4
w_b (μm)	600	$(\rho t)_{C_{60}}$ (Ω cm^2) [a]	1.1
s (mm)	0.95		

[a]Reference 37.

determined. While most of the values could be found in the literature or from the device geometry, the specific contact resistance between the ITO and copper grid had to be experimentally measured. Three different ITO strips with TLM patterns of electroplated copper were fabricated and measured, as shown in Fig. 7. Using Eqs. (11) and (12) with the data in Fig. 7(b), the average specific contact resistance and ITO sheet resistance were measured to be 117 $\mu\Omega$ cm^2 and 13.7 Ω/sq, respectively. For the resistance of the organic layers, $\rho_{pentacene}$ and $\rho_{C_{60}}$ were taken from Ref. 37. All of the parameters used for the calculations are listed in Table III.

Using Tables II and III, the various contributions to series resistance were calculated and are listed in Table IV. For the device without a grid, the total series resistance comprises of only the ITO and organic semiconductor layers and is calculated using Eq. (8). Considering only nongrid devices, most of the series resistance is contributed by the organic semiconductors (79%) for the small-area device while the ITO layer (78%) dominates for the large-area device (Table IV). This means that more power is lost in the ITO layer as the area increases. When metal grids are used for large-area solar cell devices, series resistance from the ITO (0.01 Ω cm^2) is negligible compared to the series resistance from the organic semiconductors (2.5 Ω cm^2). However, the shadow loss (130 μW/cm^2) is greater than the total resistive power loss (35 μW/cm^2) for the metal grid integrated device, which indicates excessive coverage with metal grids. Optimum grid design is achieved when the resistive power loss and the shadow loss are the same and can be obtained by making the finger electrodes narrower in width and/or wider in spacing to decrease shadowing and increase resistance.[31] The power loss associated with the contact resistance of the grid was negligible compared to other sources of power loss in the cells.

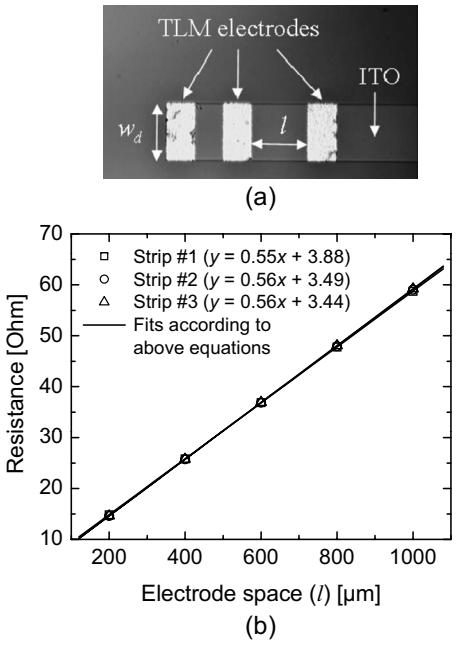

FIG. 7. (a) Micrograph of TLM test patterns on an ITO strip. w_d is the width of the electrodes and l is the space between electrodes. (b) Total contact resistance (R_{tot}) plotted for different electrode spacings on three different ITO strips. The specific contact resistance and the ITO sheet resistance are calculated from the slope, and the contact resistance is found at the intercept at l=0.

J-V characteristics of the large-area device with the metal grid along with the large-area and small-area devices without a metal grid in the dark and under illumination are shown in Fig. 8. The performance parameters for this device along with the two previously presented devices are listed in Table IV. Although the area of the grid device that is passivated with photoresist does not contact the organic layers and does not contribute photocurrent or diode current to the device, an active area of 7 cm^2 was used to calculate the photocurrent density for both the large-area devices with and without metal grids for comparison. R_SA and R_PA were calculated from the forward- and reverse-bias characteristics under illumination, respectively.

Compared to the large-area device without a metal grid, the device with a grid exhibits improved overall performance, and a significant decrease and increase in R_SA and FF are observed, respectively. A reduction in almost one order of magnitude was achieved for R_SA, thereby improving FF by more than 75%. Furthermore, J_{SC} increased from 4.5 to 4.9 mA/cm^2 even though less area contributed to the photocurrent generation because of the shadowing from the metal grids. In other words, the effective J_{SC} of the metal grid integrated device is 5.7 mA/cm^2 when only the photocurrent generating area (7 cm^2 $\times$ 85.7%=6 cm^2) is considered, which is close to the 6.0 mA/cm^2 of the small-area device. With the improved J_{SC} and FF, the power conversion efficiency is greatly increased to 0.77% compared to 0.41% for the large-area device without a grid.

The large-area device with a grid exhibited comparable performance to the small-area device in terms of FF and R_SA. FF and R_SA were 0.51 and 5.6 Ω cm^2 for the large-area device with a grid and were much closer to those of the small-area device (FF and R_SA of 0.54 and 2.8 Ω cm^2, respectively) compared to the large-area device without a grid. However, the photocurrent is still 18% lower for the device with a grid because of the shadowing from the grid. Overall, the small-area device exhibited higher power conversion efficiency than the grid device because of the higher series resistance and lower photocurrent of the grid device. In addition, nonuniform organic semiconductors associated with

TABLE IV. Experimental solar cell performance from the measurements and predicted performance from the calculation. The measured series resistance is calculated from the inverse slopes of the forward characteristics in Fig. 8.

Calculation								
A (cm^2)	Contributions to R_SA (Ω cm^2)					Shadow loss total ($\mu W/cm^2$)	J_{max} (mA/cm^2)	P_R ($\mu W/cm^2$)
	ITO	Organic	Grids	Contact	Total			
0.13	0.97	2.5	···	···	3.5	···	4.4	68
7 (no grid)	9.27	2.5	···	···	11.8	···	2.5	74
7 (with grid)	0.01	2.5	0.15	0.002	2.7	130	3.6	35

Measurement									
A (cm^2)	J_{SC} (mA/cm^2)	V_{OC} (mV)	J_{max} (mA/cm^2)	V_{max} (mV)	FF	η (%)	R_PA (Ω cm^2)	R_SA (Ω cm^2)	P_R ($\mu W/cm^2$)
0.13	6.0	401	4.4	300	0.54	1.23	361	2.8	54
7 (no grid)	4.5	338	2.5	180	0.29	0.41	157	52.1	325
7 (with grid)	4.9	342	3.6	230	0.51	0.77	429	5.6	73

Equivalent circuit model (J_0=0.01 $\mu A/cm^2$, J_{ph}=4.9 mA/cm^2, n=1.07)									
Simulated device	J_{SC} (mA/cm^2)	V_{OC} (mV)	J_{max} (mA/cm^2)	V_{max} (mV)	FF	η (%)	R_PA (Ω cm^2)	R_SA (Ω cm^2)	P_R ($\mu W/cm^2$)
With grid	4.8	340	3.3	252	0.51	0.78	199	5	54
No grid	3.9	340	2.4	184	0.34	0.42	199	50	295

larger areas may also contribute to the lower efficiency of the grid device compared to the small-area device, although uniformity studies have not yet been conducted.

According to the calculation, the series resistance of the grid device was lowest among the three devices. The grid device exhibited a 75% lower calculated series resistance compared to the large-area device without a grid, whereas there was an 89% reduction in the series resistance determined from experiment. For the large-area device without a grid, the discrepancy between measured and calculated series resistance is the largest compared to the others because of the assumption that was made when Eq. (5) was derived. It was assumed that all of the current flows in a direction normal to the edge and that this is the shortest path in a given solar cell. However, because of the point contact on each edge [Fig. 6(c)], this assumption is no longer valid. For the fabricated large-area device without a grid, photogenerated current flows toward the point interconnect contacts, which are not always perpendicular to the direction of the current flow. Thus, Eq. (5) yields lower values than the experiment because the average current path length is longer than what is assumed in the calculation. The small-area device exhibited smaller error because of its small size compared to the large-area device.

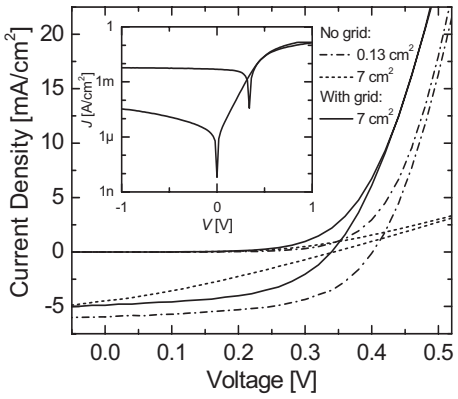

FIG. 8. Experimental J-V characteristics of the large-area device with a grid (solid) and the small-area (dashed-dot) and large-area (dashed) devices without a grid in the dark and under illumination. Inset: full-range curve for the grid device in semilogarithmic scale for comparison with the devices in Fig. 1.

As was stated before, both FF and efficiency were greatly affected by the series resistance (Fig. 3). The equivalent circuit model was simulated at the series resistance (R_SA) of 5 and 50 Ω cm^2, and the results are summarized in Table IV. The diode parameters used for this simulation were extracted from the J-V characteristic curve of the large-area device with a grid under illumination. The equivalent circuit model simulation predicted FF of 0.51 and power conversion efficiency of 0.78% when the R_SA was 5 Ω cm^2 and they were reduced to 0.34% and 0.42% when the R_SA was increased to 50 Ω cm^2. For the large-area device with a grid (R_SA=5.6 Ω cm^2), FF and efficiency were 0.51 and 0.77%, and they were 0.29 and 0.41% for the large-area device without a grid (R_SA=52.1 Ω cm^2). This indicates that the equivalent circuit model simulation and the measurement are in good agreement.

VIII. SUMMARY

In summary, area-scaling performance of organic solar cells was studied based on pentacene/C_{60} heterojunctions. Small-area devices (0.13 cm^2) were prepared as reference samples and large-area devices (7 cm^2) were fabricated with and without a grid. Various power loss contributions were

discussed and studied by means of the power loss density concept, which led to the calculation of series resistance. The equivalent circuit model was used to study the effects of the series resistance on the overall performance of organic solar cells in both small- and large-area devices.

The model fitted the experimental data well over the entire range of measurement voltages both in the dark and under illumination. The model clearly indicated that series resistance was the most impacted parameter as solar cell area increases under illumination. The series resistance increased more than 23-fold when the solar cell area increased from 0.13 to 7 cm^2. To study the effects of the series resistance increase on the overall solar cell performance, the equivalent circuit model was simulated by varying the series resistance while holding other parameters constant. The simulation showed that J_{SC} and FF were substantially lowered as series resistance was increased, thereby decreasing power conversion efficiency.

While the equivalent circuit model suggested that series resistance increased as solar cell area became large and as a result the performance parameters such as J_{SC}, FF, and η were reduced, power loss analysis helped to understand where and how much photogenerated power was lost. Furthermore, series resistance, which is independent of operating current and voltage, was easily derived from the power loss calculation and used to compare small- and large-area device performance. Provided the cathode, Al in this case, is highly conductive and thick, the analysis indicated that the series resistance contribution from the ITO was the only area-scaling component of the organic solar cell, therefore limiting power conversion efficiency as solar cell area increases. While only organic multilayer solar cells were studied in detail here, the modeling procedure can also be applied to organic bulk-heterojunction cells.

Based on the discussion above, it has been shown that the equivalent circuit model and series resistance analysis are comprehensive tools to understand the area-scaling performance of organic solar cells. Furthermore, electroplated metal grid integration with ITO was successfully demonstrated as a promising technology for large area organic solar cells by minimizing series resistance. The measurement results are well matched to the predictions of the equivalent circuit model and the power loss calculations. The developed metal grid integration platform will be useful not only for large-area single organic solar cells but also for organic solar cell modules by minimizing series resistance. While metal grids were implemented here on the large-area device (7 cm^2), the same design can be applied to much larger areas without significantly increasing resistive power loss densities by using the same grid spacing with a thicker grid. However, uniform film deposition over the large-area surface is also required for area-independent performance. The thick metal grid approach will be essential as the current density of the organic solar cell increases.

ACKNOWLEDGMENTS

The authors would like to thank Professor Ajeet Rohatgi and his research group for fruitful discussions. This material is based upon the work supported in part by the STC Program of the National Science Foundation under Agreement No. DMR-0120967 and by the Office of Naval Research. This work was performed in part at the Microelectronics Research Center at Georgia Institute of Technology, a member of the National Nanotechnology Infrastructure Network, which is supported by NSF (Grant No. ECS-03-35765).

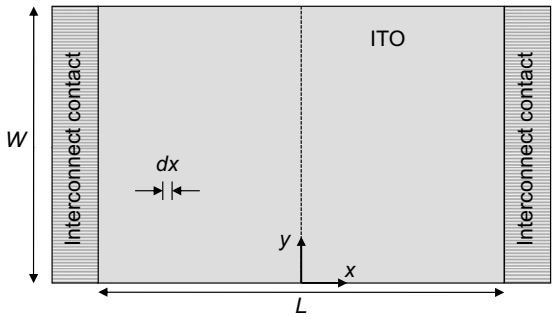

FIG. 9. Solar cell with interconnect contacts. Total area of the cell is *LW*.

APPENDIX: ITO POWER LOSS DENSITY CALCULATION

The power loss in the unit cell associated with the current which flows through the ITO layer is given as

$$p_{\mathrm{ITO}} = \int I_{\max}^2 dR, \tag{A1}$$

where I is the lateral current which flows normal to the interconnect contacts (Fig. 9),

$$I_{\max} = J_{\max} W x. \tag{A2}$$

The incremental resistance in the section dx is given by

$$dR = R_{\text{sheet-ITO}} \frac{dx}{W}, \tag{A3}$$

where $R_{\text{sheet-ITO}}$ is the sheet resistance of the ITO in Ω/sq. Combining Eqs. (A1)–(A3), the power loss in the unit cell with one interconnect contact at the edge is given by

$$p_{\mathrm{ITO}} = \left[\int_0^L (J_{\max} W x)^2 R_{\text{sheet-ITO}} \frac{dx}{W} \right], \tag{A4}$$

$$= J_{\max}^2 W R_{\text{sheet-ITO}} \int_0^L x^2 dx, \tag{A5}$$

$$= \frac{1}{3} J_{\max}^2 L^3 W R_{\text{sheet-ITO}} \ [\mathrm{mW}]. \tag{A6}$$

Therefore, the power loss density at the maximum power point is given by

$$P_{\mathrm{ITO}} = \frac{p_{\mathrm{ITO}}}{\text{unit cell area}} = \frac{\frac{1}{3} J_{\max}^2 L^3 W R_{\text{sheet-ITO}}}{LW}, \tag{A7}$$

$$P_{\mathrm{ITO}} = \frac{1}{3} J_{\max}^2 L^2 R_{\text{sheet-ITO}} \ [\mathrm{mW\ cm^2}]. \tag{A8}$$

If both interconnect contacts on the edges are used, then Eq. (A4) is modified as

$$p_{\mathrm{ITO}} = \left[2\int_0^{L/2} (J_{\max} W x)^2 R_{\text{sheet-ITO}} \frac{dx}{W} \right], \tag{A9}$$

$$= \frac{1}{12} J_{\max}^2 L^3 W R_{\text{sheet-ITO}} \ [\mathrm{mW}]. \tag{A10}$$

Therefore, the power loss density when both interconnect contacts are used is given by

$$P_{\mathrm{ITO}} = \frac{p_{\mathrm{ITO}}}{\text{unit cell area}} = \frac{\frac{1}{12} J_{\max}^2 L^3 W R_{\text{sheet-ITO}}}{LW}, \tag{A11}$$

$$P_{\mathrm{ITO}} = \frac{1}{12} J_{\max}^2 L^2 R_{\text{sheet-ITO}} \ [\mathrm{mW\ cm^2}]. \tag{A12}$$

Note that by utilizing interconnect contacts on both edges, the power loss density is reduced by fourfold compared to single interconnect contact design.

[1] B. Kippelen and J.-L. Bredas, Energy Environ. Sci. **2**, 251 (2009).
[2] C. J. Brabec and J. R. Durrant, MRS Bull. **33**, 670 (2008).
[3] G. Dennler, M. C. Scharber, and C. J. Brabec, Adv. Mater. (Weinheim, Ger.) **21**, 1323 (2009).
[4] R. Kroon, M. Lenes, J. C. Hummelen, P. W. M. Blom, and B. de Boer, Polym. Rev. **48**, 531 (2008).
[5] T. Ameri, G. Dennler, C. Lungenschmied, and C. J. Brabec, Energy Environ. Sci. **2**, 347 (2009).
[6] D. Gupta, M. Bag, and K. S. Narayan, Appl. Phys. Lett. **93**, 163301 (2008).
[7] A. K. Pandey, J. M. Nunzi, B. Ratier, and A. Moliton, Phys. Lett. A **372**, 1333 (2008).
[8] S. Yoo, B. Domercq, and B. Kippelen, Appl. Phys. Lett. **85**, 5427 (2004).
[9] S. Yoo, B. Domercq, and B. Kippelen, J. Appl. Phys. **97**, 103706 (2005).
[10] A. R. McGhie, A. F. Garito, and A. J. Heeger, J. Cryst. Growth **22**, 295 (1974).
[11] W. J. Potscavage, Jr., S. Yoo, and B. Kippelen, Appl. Phys. Lett. **93**, 193308 (2008).
[12] A. C. Mayer, M. T. Lloyd, D. J. Herman, T. G. Kasen, and G. G. Malliaras, Appl. Phys. Lett. **85**, 6272 (2004).
[13] A. K. Pandey and J.-M. Nunzi, Appl. Phys. Lett. **89**, 213506 (2006).
[14] A. Cheknane, H. S. Hilal, F. Djeffal, B. Benyoucef, and J.-P. Charles, Microelectron. J. **39**, 1173 (2008).
[15] W. U. Huynh, J. J. Dittmer, N. Teclemariam, D. J. Milliron, A. P. Alivisatos, and K. W. J. Barnham, Phys. Rev. B **67**, 115326 (2003).
[16] A. Cheknane, B. Benyoucef, J. P. Charles, R. Zerdoum, and M. Trari, Sol. Energy Mater. Sol. Cells **87**, 557 (2005).
[17] J. M. Nunzi, *Organic Materials and Devices for Photovoltaic Applications* (Kluwer, Dordrecht, 2002), pp. 197–224.
[18] D. L. Meier and D. K. Schroder, IEEE Trans. Electron Devices **31**, 647 (1984).
[19] H. B. Serreze, Conference Record of the IEEE Photovoltaic Specialists Conference, 1978 (unpublished), pp. 609–614.
[20] R. W. Miles, K. M. Hynes, and I. Forbes, Prog. Cryst. Growth Charact. Mater. **51**, 1 (2005).
[21] D. Wöhrle, L. Kreienhoop, G. Schnurpfeil, J. Elbe, B. Tennigkeit, S. Hiller, and D. Schlettwein, J. Mater. Chem. **5**, 1819 (1995).
[22] V. Bulovic, P. E. Burrows, D. Z. Garbuzov, M. E. Thompson, A. G. Tsekoun, and S. R. Forrest, AIP Conf. Proc. **404**, 235 (1997).
[23] J. Xue, S. Uchida, B. P. Rand, and S. R. Forrest, Appl. Phys. Lett. **84**, 3013 (2004).
[24] C.-J. Ko, Y.-K. Lin, F.-C. Chen, and C.-W. Chu, Appl. Phys. Lett. **90**, 063509 (2007).
[25] C.-H. Lin, S.-C. Tseng, Y.-K. Liu, Y. Tai, S. Chattopadhyay, C.-F. Lin, J.-H. Lee, J.-S. Hwang, Y.-Y. Hsu, L.-C. Chen, W.-C. Chen, and K.-H. Chen, Appl. Phys. Lett. **92**, 233302 (2008).
[26] P. Peumans and S. R. Forrest, Appl. Phys. Lett. **79**, 126 (2001).
[27] T. Aernouts, P. Vanlaeke, W. Geens, J. Poortmans, P. Heremans, S. Borghs, R. Mertens, R. Andriessen, and L. Leenders, Thin Solid Films **451–452**, 22 (2004).
[28] M. Glatthaar, M. Niggemann, B. Zimmermann, P. Lewer, M. Riede, A. Hinsch, and J. Luther, Thin Solid Films **491**, 298 (2005).
[29] O. I. K. Tvingstedt, Adv. Mater. **19**, 2893 (2007).
[30] M.-G. Kang, M.-S. Kim, J. Kim, and L. Jay Guo, Adv. Mater. (Weinheim, Ger.) **20**, 4408 (2008).
[31] M. A. Green, *Solar Cells* (Prentice-Hall, Englewood Cliffs, NJ, 1982).
[32] D. K. Schroder, *Semiconductor Material and Device Characterization* (Wiley-Interscience, Hoboken, NJ, 1990).
[33] D.-J. Yun, D.-K. Lee, H.-K. Jeon, and S.-W. Rhee, Org. Electron. **8**, 690 (2007).
[34] J. Y. Park and M. G. Allen, IEEE Trans. Electron. Packag. Manuf. **23**, 48 (2000).
[35] A. Sharma, B. Kippelen, P. J. Hotchkiss, and S. R. Marder, Appl. Phys. Lett. **93**, 163308 (2008).
[36] F. Nuesch, L. J. Rothberg, E. W. Forsythe, Q. T. Le, and Y. Gao, Appl. Phys. Lett. **74**, 880 (1999).
[37] A. Haldi, A. Sharma, W. J. Potscavage, Jr., and B. Kippelen, J. Appl. Phys. **104**, 064503 (2008).